IEEE Access
Multidisciplinary | Rapid Review | Open Access Journal

Received August 19, 2019, accepted August 28, 2019, date of publication September 3, 2019,
date of current version September 18, 2019.

Digital Object Identifier 10.1109/ACCESS.2019.2939148

Accurate and Robust Synchronous Extraction Algorithm for Star Centroid and Nearby Celestial Body Edge

YONG ZHANG[1,2], JIE JIANG[1,2], GUANGJUN ZHANG[1,2], AND YAN LU[1]

[1]School of Instrumentation and Opto-Electronics Engineering, Beihang University, Beijing 100191, China
[2]Key Laboratory of Precision Opto-Mechatronics Technology, Ministry of Education, Beijing Advanced Innovation Center for Big Data-Based Precision Medicine, Beihang University, Beijing 100191, China

Corresponding author: Jie Jiang (jiangjie@buaa.edu.cn)

This work was supported by the National Neural Science Foundation of China 61725501.

ABSTRACT Celestial body features are important navigation information in deep space exploration. This study provides a synchronous high-precision extraction algorithm for star centroid and nearby celestial body edges for a miniaturized independent optical navigation sensor, which combines the functions of a star tracker and a navigation camera. The image is filtered by a ring filter template to eliminate the interference information of background and improve the contrast between the target and the background. The second-order directional derivative and specific area characteristic method aim to roughly extract and distinguish the features (star centroid and the nearby celestial body edge). In local area template where feature points are located, the 1D energy deviation effect is proposed to extract the features of the two different light intensity distribution models. The accuracy and robustness of our algorithm are verified by simulation and ground-based experiments. The algorithm has certain reference significance for other types of dim target and edge detections, such as infrared detection, medical image, target measurement, and machine vision.

INDEX TERMS Optical autonomous navigation, high robustness and accuracy, star centroid, nearby celestial body edge, 1D energy deviation effect.

I. INTRODUCTION

Deep-space autonomous navigation can achieve tasks, such as orbit determination and control, attitude orientation, and target tracking, in the event of loss of ground communication; thus, it greatly enhances the survivability of the spacecraft [1]. Autonomous navigation technology used in several representative missions and plans of deep space exploration shows that the current mainstream autonomous navigation technology of deep space exploration is based on the image information of navigation star or target celestial body obtained by optical autonomous navigation (OPNAV) sensor [2], [3].

OPNAV acquires the attitude and navigation information of the spacecraft by processing the target celestial body image. Two navigation target objects are expected to appear simultaneously in a typical image acquired by optical sensors. The first type of object is a star that appears as a point source in a focused image, the second type of object is a nearby celestial body (such as a planet or moon) that illuminates many pixels in the image [4]. The star can determine the attitude of the spacecraft [5], [6]. The nearby celestial body can provide some navigation information, including line-of-sight (LOS) vector, apparent diameter and center of mass, and the angle between horizon and reference star [7].

The existing star centroid extraction methods mainly include centroid and Gaussian fitting [8]–[11]. The centroid method is the ratio of the first moment of the star light intensity to the zero moment of the pixel coordinate and is sensitive to the high frequency noise. The Gaussian fitting method is based on the principle that the star imaging obeys the 2D Gaussian distribution and involves a large amount of calculation. The nearby celestial body imaging is relatively large. The current mainstream idea is to extract the edge pixels of the contour and then fit the center and radius. The Canny operator is used to extract the edge of the nearby celestial body but only achieves pixel-level precision [7], [12]–[14]. The Zernike moment is used to extract the sub-pixel edge of the nearby celestial body, which is computationally intensive [15], [16]. If the blurred edge model is considered, then the model parameters will be increased, thereby bringing

The associate editor coordinating the review of this article and approving it for publication was Abdullah Iliyasu.

difficulty in determining the analytical solution. These feature (star centroid and edge of the nearby celestial body) extraction methods can only obtain navigation information of a single celestial body.

The traditional optical navigation sensor system platform uses a rigid connection between the star tracker and the optical navigation camera [17], [18]. Light-small is the development direction of future OPNAV systems [19]–[21]. This requires the OPNAV systems to have multiple functions, one of which is a combination of a star tracker and a navigation camera. In [20], a scheme for simultaneous imaging of star and nearby celestial body based on well capacity adjusting was provided. Therefore, simultaneously extract different celestial features is very important. Jiang *et al.* first proposed the concept of synchronous extraction to simultaneously obtain the navigation measurement of the star and the nearby celestial body [21]. Sub-pixel extraction of feature points was implemented based on the improved Hessian matrix method, but the second derivative was sensitive to noise and the calculation was complicated.

Therefore, the current study proposes a high accuracy synchronous extraction algorithm for star and nearby celestial body features. The algorithm mainly consists of three parts: 1) Ring filter template is used to filter the image; 2) Features are extracted and distinguished based on second-order directional derivative (SDD) and specific area characteristics; 3) Sub-pixel features in the local area template are extracted using 1D energy deviation effect.

The remainder of the paper is organized as follows. Section 2 establishes the light intensity models of star and nearby celestial body. Section 3 describes the synchronization extraction algorithm for star and nearby celestial body in detail. Section 4 presents the experimental results and discussion. Section 5, elaborates the conclusions of our work.

II. LIGHT INTENSITY MODELS FOR OBSERVED OBJECTS

A. SIMULATION OF STAR

The centroid accuracy of single -pixel imaging does not meet the requirements of attitude measurement. Therefore, the defocus method is usually used to spread the star energy to multiple pixels [22], [23].

In general, the light intensity distribution of a star can be approximated as a 2D Gaussian distribution [24]–[27]:

$$G_{star}(x,y) = N_{star} * PSF(x,y) = \frac{N_{star}}{2\pi\sigma_{PSF}^2} exp\left[-\frac{(x-x_i)^2+(y-y_i)^2}{2\sigma_{PSF}^2}\right] \quad (1)$$

where $PSF(x,y)$ represents the point spread function of the optical system. (x_i, y_i) represents the star centroid coordinates. σ_{PSF} is the Gaussian diffusion radius, and more than 95% of the energy is concentrated in the area of 3×3 pixels when $\sigma_{PSF} < 0.671$. $*$ represents the 2D convolution operation. N_{star} is the number of photoelectrons generated by the star and is given by [4]

$$N_{star} = (QE)(F)\,\Upsilon_0 \tau \frac{\pi}{4} d_{ap}^2 10^{-0.4m} cos\theta\,(\Delta\lambda)\,(\Delta t) \quad (2)$$

QE is the quantum efficiency of the image sensor, F is the fill factor(the percentage of the pixel area that contains a photosensitive surface), Υ_0 is the spectral irradiance of a zero-magnitude star, τ is the transmittance of the optics, d_{ap} is the aperture diameter, $\Delta\lambda$ is the spectral range of interest, m is the star visual magnitude, and θ is the angle between the boresight direction and the i-th LOS direction. Δt is the exposure time over which photons are accumulated. The light intensity model of star is shown in Fig. 1(a).

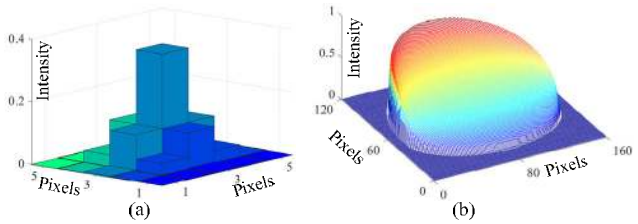

FIGURE 1. (a) Light intensity model of star; (b) light intensity model of nearby celestial body.

B. SIMULATION OF NEARBY CELESTIAL BODY

Establishing a nearby celestial body imaging model needs to determine how light is reflected from each observation point and the number of photons hitting the corresponding pixel on the detector. By calculating the number of photoelectrons on each illuminated pixel, the light intensity model of a nearby celestial body image can be established [4].

$$N_{planet} = (QE)(F)\,SA_{pixel}\,(\Delta t) \quad (3)$$

where A_{pixel} is a single-pixel area, and S is the total photon flux hitting the pixel.

$$S = I\tau\frac{\pi}{4}\left(\frac{d_{ap}}{f}\right)^2 cos^4\theta_0 \quad (4)$$

where I is the radiance of the reflected light and f is equal to the focal length. θ_0 is the angle between the LOS vector and the observer patch surface normal. The nearby celestial body imaging model is expressed as the convolution of the cumulative energy distribution of the optical system with the PSF:

$$G_{planet}(x,y) = N_{planet} * PSF(x,y) = \frac{N_{planet}}{2\pi\sigma_{PSF}^2} exp\left[-\frac{(x-x_i)^2+(y-y_i)^2}{2\sigma_{PSF}^2}\right] \quad (5)$$

The nearby celestial body imaging model is shown in Fig. 1(b), edge blur width is generally 3-5 Pixels [15], [20]. The contour of nearby celestial body imaging is composed of two arcs: circular and elliptical [28]. Only the edge of the circular arc extracted to fit the center of the nearby celestial body [7], [15].

III. SYNCHRONOUS EXTRACTION OF STAR AND NEARBY CELESTIAL BODY FEATURES

In this section, we propose a synchronous high-precision extraction algorithm for star centroid and nearby celestial body edge. First, the ring filter template is used to remove interference information and highlight feature points. Then, according to the SDD and specific area characteristics, the features are initially extracted and distinguished. Finally, the sub-pixel-level precision of the features is simultaneously extracted using 1D energy deviation effect in the local area template. The 1D energy deviation effect is based on the Gaussian function model of the light intensity distribution of the pixel where the feature point is located, combined with the relationship between the gray scale and the area on both sides of the feature point. At the same time, the local area template has a good additive cancellation effect on noise.

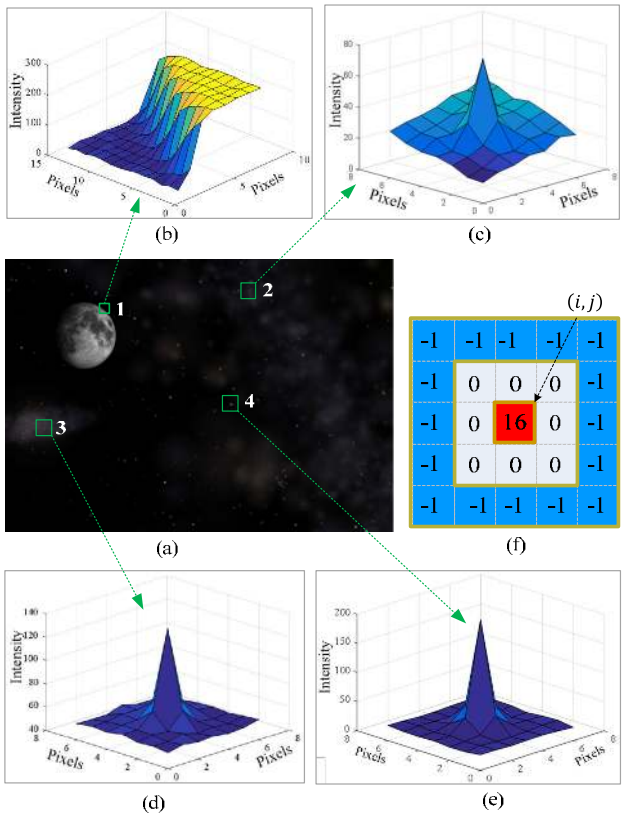

FIGURE 2. (a) Original image; (b) light intensity distribution in the edge region of the nearby celestial body; (c)-(e) light intensity distribution of Stars 2, 3, and 4, respectively; (f) ring filter template.

A. IMAGE FILTERING

Typical images often contain irregular backgrounds, such as noise, nebulae, and stray light [29], [30], as shown in Fig. 2(a). This interference information in the background severely affects the selection of stars and background segmentation thresholds. As a result, the false alarm rate of star extraction sharply rises.

The light intensity distribution in the edge region of the nearby celestial body is shown in Fig. 2(b). Fig. 2(c), Fig. 2(d), and Fig. 2(e) show the light intensity distribution of Stars 2, 3, and 4, respectively. The background of these stars can be approximated as a 2D linear plane distribution.

Fig. 2(f) shows the ring filter template $\boldsymbol{T_{ring}}$, which is convolved with the original image. The size of $\boldsymbol{T_{ring}}$ $(\boldsymbol{N}+\boldsymbol{2}) \times (\boldsymbol{N}+\boldsymbol{2})$ pixels is determined by the size of feature points $\boldsymbol{N} \times \boldsymbol{N}$ pixels. Take $\boldsymbol{N}=\boldsymbol{3}$ pixels as an example.

$$I_{conv} = I * T_{ring} \tag{6}$$

$$I_{conv}(i,j) = 16 \cdot I(i,j) - \sum\nolimits_{m,n \in \Omega_{blue}} I(m,n) \tag{7}$$

I_{conv} represents the matrix after convolution, I represents the 2D matrix form of original image, $*$ is a convolution symbol, $I(i,j)$ represents the gray value of the coordinates (i,j) in the original image, $I_{conv}(i,j)$ represents the value after convolution, and Ω_{blue} represents the blue area.

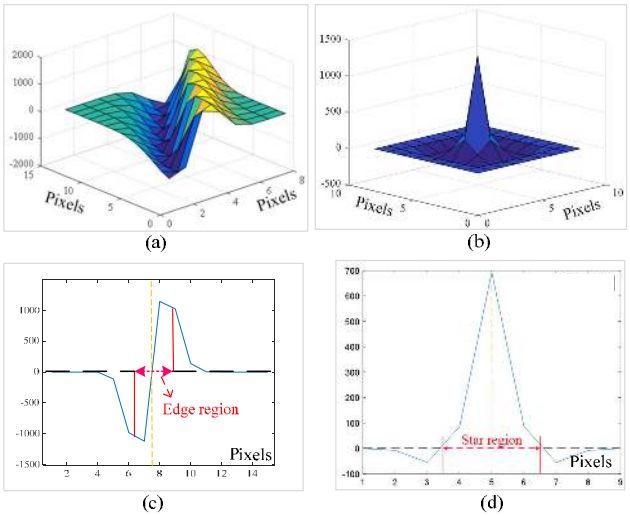

FIGURE 3. (a) Light intensity expansion value distribution of edge; (b) light intensity expansion value distribution of star; (c) 1D light intensity expansion value distribution in the gradient direction of the edge; (d) 1D light intensity expansion value distribution in the arbitrary direction of the star centroid.

Fig. 3(a) shows the light intensity expansion value distribution after convolution of Fig. 2(b). Fig. 3(b) presents the light intensity expansion value distribution after the convolution of Stars 2, 3, and 4. Fig. 3(c) exhibits the 1D light intensity expansion value distribution in the gradient direction of the edge in Fig. 3(a), and Fig. 3(d) displays the 1D light intensity expansion value distribution in the arbitrary direction of the star centroid in Fig. 3(b). After the convolution, the light intensity of the surface region of the nearby celestial body is 0 (excluding the surface texture). In addition, interference information in the background is largely eliminated. The intensity of the features (star and the edge of nearby celestial body) is also significantly expanded, which is beneficial to extraction.

B. FEATURE ROUGH EXTRACTION BASED ON SDD AND SPECIFIC AREA CHARACTERISTICS

The following is a rough extraction of features, which is mainly based on SDD and specific area characteristics.

1) SDD

The theory of SDD is used in the field of small targets and edge detection. [31], [32]. The SDD of any point (x, y) in I_{conv} is:

$$\frac{d^2 I_{conv}}{d\theta^2} = \frac{1}{2}\left(\frac{\partial^2 I_{conv}}{\partial x^2} + \frac{\partial^2 I_{conv}}{\partial y^2}\right) + \frac{1}{2}\left(\frac{\partial^2 I_{conv}}{\partial x^2}\frac{\partial^2 I_{conv}}{\partial y^2}\right) \times cos2\theta + \frac{1}{2}\left(\frac{\partial^2 I_{conv}}{\partial x \partial y} + \frac{\partial^2 I_{conv}}{\partial y \partial x}\right) sin2\theta \quad (8)$$

The maximum *SDD* of (x, y) is SDD_{max}:

$$SDD_{max} = \left(\frac{d^2 I_{conv}}{d\theta^2}\right)_{max} = \frac{1}{2}\left(\frac{\partial^2 I_{conv}}{\partial x^2} + \frac{\partial^2 I_{conv}}{\partial y^2}\right) + \frac{1}{2}\sqrt{\left(\frac{\partial^2 I_{conv}}{\partial x^2} - \frac{\partial^2 I_{conv}}{\partial y^2}\right)^2 + \left(\frac{\partial^2 I_{conv}}{\partial x \partial y} + \frac{\partial^2 I_{conv}}{\partial y \partial x}\right)^2} \quad (9)$$

The minimum *SDD* of (x, y) is SDD_{min}:

$$SDD_{min} = \left(\frac{d^2 I_{conv}}{d\theta^2}\right)_{min} = \frac{1}{2}\left(\frac{\partial^2 I_{conv}}{\partial x^2} + \frac{\partial^2 I_{conv}}{\partial y^2}\right) - \frac{1}{2}\sqrt{\left(\frac{\partial^2 I_{conv}}{\partial x^2} - \frac{\partial^2 I_{conv}}{\partial y^2}\right)^2 + \left(\frac{\partial^2 I_{conv}}{\partial x \partial y} + \frac{\partial^2 I_{conv}}{\partial y \partial x}\right)^2} \quad (10)$$

According to SDD_{max} and SDD_{min} of I_{conv}, the region where the point is located is determined as a point distribution (star and noise) or a linear distribution (edge of nearby celestial body and its surface texture).

(a) If $SDD_{max}(x, y) < 0$, then all *SDD* at this point are less than 0 and belong to the convex region (point distribution); if $SDD_{min}(x, y) > 0$, then all *SDD* at this point are greater than 0 and belong to the concave region;

(b) When the light intensity changes uniformly, the value of *SDD* is 0. If $SDD_{max}(x, y) = 0$ and $SDD_{min}(x, y) = 0$, then the point may be the background, the edge, or surface texture of the nearby celestial body.

2) SPECIFIC AREA CHARACTERISTICS

The target feature coordinate are also selected depending on the distribution characteristics of I_{conv} and its SDD on a specific area. The $N \times N$ pixels around the star are taken as star's specific areas of star T_s, and $(N+2) \times (N+2)$ pixels around the edge are taken as specific areas of nearby celestial body edge T_c. Take $N = 3$ pixels as an example.

(a) If at least four pixels in T_s satisfy $I_{conv}(i, j) > (\tau'_{bg} + 50)$, then the point is the pixel where the star centroid is located; otherwise, it is noise. τ'_{bg} is the global background threshold and is determined by the multi-window sampling method [21].

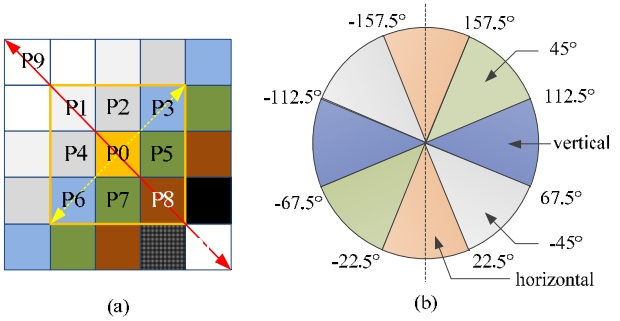

FIGURE 4. (a) Edge specific areas; (b) four types of edges.

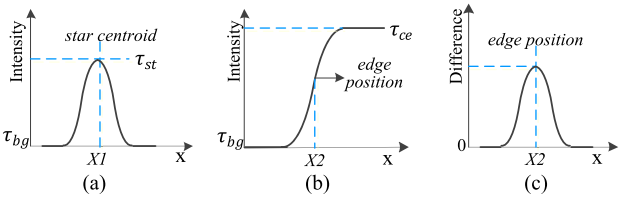

FIGURE 5. 1D light intensity distribution of star and edge. (a) light intensity distribution model in arbitrary direction of the star centroid; (b) light intensity distribution model in gradient direction of edge; (c) light intensity difference model in gradient direction of the edge.

(b) Fig. 4(a) presents the specific areas where the edge pixel P0 is located. The gradient direction of P0 is d_{P0}. Fig. 4(b) shows that the edges are grouped into four types according to d_{P0}: horizontal, $-45°$, vertical, and $45°$.

Fig. 4(a) shows an example in which the edge direction is 45° (yellow line), and P3 and P6 are approximate edge pixel points; P1 and P8 are the pixels in the gradient direction (red line). Black pixels are background, white pixels are targets, and other color pixels are edge blurred areas. The SDD_{max} and SDD_{min} of P1 − P8 in I_{conv} are analyzed. SDD_{min} of P1 is the smallest, SDD_{max} of P8 is the largest, and $SDD_{max}(P8) \approx |SDD_{min}(P1)|$. The point satisfying these conditions is the edge pixel (including the contour edge and surface texture edges). Finally, the pixel points P9 and P10 in the gradient direction of the original image are analyzed. If P9 $> \tau_{edge}$ and P10 $< \tau_{bg}$, then it is the circular arc edge point of the nearby celestial body. τ_{edge} is the circular arc edge threshold, which satisfies $\tau_{edge} = [max(I_{edge}) + min(I_{edge})]/2$, I_{edge} is the gray value of the edge point in the original image. τ_{bg} is the background threshold of the original image and is determined by the multi-window sampling method.

C. SUB-PIXEL FEATURE EXTRACTION BASED ON 1D ENERGY DEVIATION EFFECT

The pixel-level star centroid and the nearby celestial body circular arc edge are extracted and then positioned at the sub-pixel level. In Fig. 5(a), X1 is 1D star centroid and τ_{st} represents the maximum intensity of star. The 1D light intensity distribution of the nearby celestial body in the gradient direction satisfies blurred edge model [33]–[35]. In Fig. 5(b), X2 represents the edge position and τ_{ce} represents light intensity of nearby celestial body. Fig. 5(c) shows the light

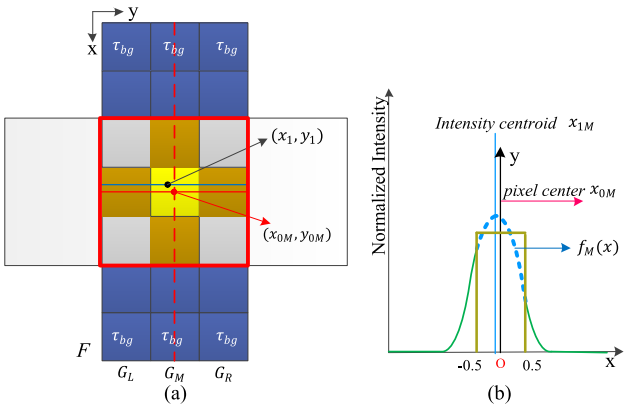

FIGURE 6. (a) Local area template of star; (b) 1D light intensity normalized distribution of the G_M column.

intensity difference distribution in gradient direction of the edge.

Sub-pixel position is generally determined by the integer pixel position around the pixel. Therefore, we propose a 1D energy deviation effect method in the local area template to extract sub-pixel features. We are the first to use 1D model for simultaneously processing 2D images of two celestial bodies with two different light intensity distributions. Select the $(N+4)\times 3$ vertical or $3\times(N+4)$ horizontal pixels area as the local area template where the features are located. Take $N=3$ pixels as an example.

1) STAR SUB-PIXEL CENTROID EXTRACTION

In Fig. 6(a), (x_1, y_1) is the true centroid of the star. The vertical and horizontal local area templates are used to solve x_1 and y_1, respectively. For a vertical 7×3 pixels template as an example, G_L, G_M, and G_R represent the left, middle, and right columns, respectively. The center pixel coordinate of the G_M column is (x_{0M}, y_{0M}). Fig. 6(b) shows the 1D light intensity normalized distribution of the G_M column, which satisfies the 1D Gaussian function probability density function:

$$f_M(x) = \frac{1}{\sigma(2\pi)^{1/2}} exp\left(-\frac{(x-x_{1M})^2}{2\sigma^2}\right) \tag{11}$$

x_{1M} represents G_M column 1D intensity center. $f_M(x)$ is symmetric about x_{1M} axis:

$$\int_{x_{0M-3.5}}^{x_{1M}} f_M(x)dx = \int_{x_{1M}}^{x_{0M}+3.5} f_M(x)\,dx \tag{12}$$

x_{0M} represents the center of the pixel.

where:

$$\int_{x_{0M-3.5}}^{x_{1M}} f(x)\,dx = \sum_{i=-1}^{-3} F_M(x_{0M}+i, y_{0M}) + \int_{x_{0M-0.5}}^{x_{1M}} f_M(x)dx \tag{13}$$

$$\int_{x_{1M}}^{x_{0M}+3.5} f_M(x)dx = \sum_{i=1}^{3} F_M(x_{0M}+i, y_{0M}) + \int_{x_{1M}}^{x_{0M}+0.5} f_M(x)dx \tag{14}$$

where $F_M(x,y)$ represents the normalized gray value of the G_M column. $\sum_{i=-1}^{-3} F_M(x_{0M}+i, y_{0M})$ and $\sum_{i=1}^{3} F_M(x_{0M}+i, y_{0M})$ represent the sum of the gray values of the three pixels above and below the (x_{0M}, y_{0M}) in the G_M column, respectively. The 1D energy deviation effect between the left and right sides of the center pixel is ΔE_M:

$$\begin{aligned}\Delta E_M &= \int_{x_{0M-0.5}}^{x_{1M}} f_M(x)\,dx - \int_{x_{1M}}^{x_{0M}+0.5} f_M(x)\,dx \\ &= \sum_{i=1}^{3} F_M(x_{0M}+i, y_{0M}) - \sum_{i=-1}^{-3} F_M(x_{0M}+i, y_{0M})\end{aligned} \tag{15}$$

The pixel gray value at (x_{0M}, y_{0M}) is expressed as

$$F_M(x_{0M}, y_{0M}) = \int_{-0.5}^{0.5} f_M(x)\,dx = \Phi\left(\frac{0.5-x_{1M}}{\sigma}\right) - \Phi\left(\frac{-0.5-x_{1M}}{\sigma}\right) \tag{16}$$

where $\Phi(x)$ represents the cumulative distribution function:

$$\Phi(x) = \int_{-\infty}^{x} f_M(x)dx \tag{17}$$

Then, ΔE_M satisfies

$$\begin{aligned}\Delta E_M &= \int_{-0.5}^{x_{1M}} f_M(x)\,dx - \int_{x_{1M}}^{0.5} f_M(x)\,dx = 2\Phi(0) \\ &= -\Phi\left(\frac{=0.5-x_{1M}}{\sigma}\right) - \Phi\left(\frac{-0.5-x_{1M}}{\sigma}\right) \\ &= \sum_{i=1}^{3} F_M(x_{0M}+i, y_{0M}) - \sum_{i=-1}^{-3} F_M(x_{0M}+i, y_{0M})\end{aligned} \tag{18}$$

where (19) and (20), as shown at the bottom of this page.

From the standard normal distribution function table, $\Phi(0) = 0.5$. The values of $\frac{0.5-x_{1M}}{\sigma}$ and $\frac{-0.5-x_{1M}}{\sigma}$ also can

$$\Phi\left(\frac{0.5-x_{1M}}{\sigma}\right) = \frac{2\Phi(0) - \sum_{i=1}^{3} F_M(x_{0M}+i, y_{0M}) + \sum_{i=-1}^{-3} F_M(x_{0M}+i, y_{0M}) + F_M(x_{0M}, y_{0M})}{2} \tag{19}$$

$$\Phi\left(\frac{-0.5-x_{1M}}{\sigma}\right) = \frac{2\Phi(0) - \sum_{i=1}^{3} F_M(x_{0M}+i, y_{0M}) + \sum_{i=-1}^{-3} F_M(x_{0M}+i, y_{0M}) + F_M(x_{0M}, y_{0M})}{2} \tag{20}$$

be obtained. For convenience of description, we make

$$\begin{cases} \dfrac{0.5 - x_{1\mathrm{M}}}{\sigma} = data1 \\ \dfrac{-0.5 - x_{1\mathrm{M}}}{\sigma} = data2 \end{cases} \tag{21}$$

Then

$$x_{1M} = -\frac{data1 + data2}{2\,(data1 - data2)} \tag{22}$$

The light intensity distribution of G_L and G_R column also satisfies the 1D Gaussian distribution. We use the method of solving x_{1M} to find the energy centers x_{1L} and x_{1R} of the G_L column and the G_R column, respectively. Then, the centroid of the x-axis of the star is

$$x_1 = (x_{1L} + x_{1M} + x_{1R})/3 \tag{23}$$

Similar to the method of solving x_1, we select the horizontal direction 3×7 pixels as the local area template to find the star centroid y_1 on the y-axis.

$$y_1 = (y_{1T} + y_{1C} + y_{1B})/3 \tag{24}$$

In the horizontal template, y_{1T}, y_{1C}, and y_{1B} are three rows of energy centers, respectively. The true centroid of the star (x_1, y_1) has been obtained.

2) NEARBY CELESTIAL BODY SUB-PIXEL EDGE EXTRACTION

If the edge gradient direction belongs to [45°, 135°) or [−135°, −45°) when extracting nearby celestial body sub-pixel edges, then we select horizontal 3×7 pixels as local area template. Otherwise, we select vertical 7×3 pixels as local area template. We will use a vertical template as an example.

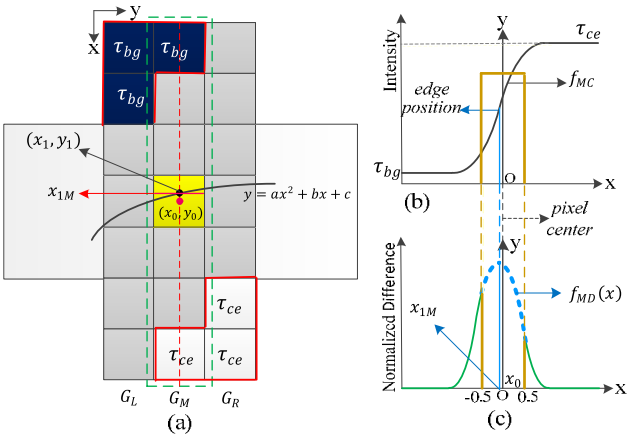

FIGURE 7. (a) Local area template of nearby celestial body edge; (b) 1D light intensity distribution of the G_M column; (c) light intensity differential normalized distribution of G_M columns.

In Fig. 7(a), the edge pixel coordinate is (x_0, y_0); the true sub-pixel edge coordinate is (x_1, y_1); and G_L, G_M, and G_R represent the left, middle, and right columns, respectively. Fig. 7(b) shows the 1D light intensity distribution of the G_M column, which satisfies the function

$$f_{MC}(x) = \frac{\tau_{ce} - \tau_{bg}}{2}\left(erf\left(\frac{x - x_{1M}}{\sqrt{2}\sigma}\right) + 1\right) + \tau_{bg} \tag{25}$$

where τ_{ce} and τ_{bg} represent the gray value of the target and background, respectively. x_{1M} represents the center of the 1D light intensity distribution. The function $erf(x)$ is defined as

$$erf(x) = \frac{2}{\sqrt{\pi}}\int_0^x e^{-t^2}dt \tag{26}$$

Fig. 7(c) shows the G_M column intensity differential normalized distribution, and the average of the forward and backward differences is selected as the gray difference value. The intensity differential normalized distribution $f_{MD}(x)$ also satisfies the 1D Gaussian function probability density function:

$$f_{MD}(x) = \frac{1}{\sigma(2\pi)^{1/2}}\exp\left(-\frac{(x - x_{1M})^2}{2\sigma^2}\right) \tag{27}$$

Using Formulas (12)–(22) to calculate the 1D energy deviation effect for the three columns G_L, G_M, and G_R, three preliminary sub-pixel positions $x_{1\mathrm{L}}$, $x_{1\mathrm{M}}$, and $x_{1\mathrm{R}}$ can be obtained.

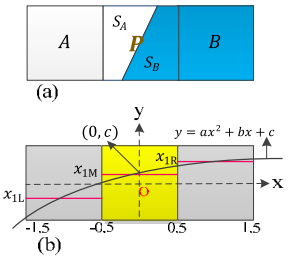

FIGURE 8. (a) Edge pixel gray value proportional to the intensity and area on the two sides of the edge; (b) edge approximated by a second-order curve.

Unlike the 2D light intensity distribution of star, edge pixels do not satisfy the principle of isotropic. The pixel gray value is determined by the gray value and area of the two sides of the edge. In Fig. 8(a), the linear edge segmentation pixel P is divided into two parts: S_A and S_B. The gray values on the two sides of the edge are A and B, respectively. Then, the gray value of the pixel is [36]

$$g_P = \frac{A * S_A + B * S_B}{S_A + S_B} \tag{28}$$

In Fig. 8(b), $x_{1\mathrm{L}}$, $x_{1\mathrm{M}}$, and $x_{1\mathrm{R}}$ are sub-pixel-level initial values of the edges in three columns. The edge model is a linear function parallel to the x-axis, but the real edge approximates a quadratic function: $y = ax^2 + bx + c$. The area ratio of the edge segmentation pixels is the same regardless of a linear function edge or a highly realistic quadratic function edge because the pixel gray value is determined and the gray distribution on the two sides is the same. Specifically,

$$\int_{-1.5}^{-0.5}(ax^2 + bx + c + 0.5)dx = \int_{-1.5}^{-0.5}(x_{1L} + 0.5)dx \tag{29}$$

$$\int_{-0.5}^{0.5}(ax^2+bx+c+0.5)dx=\int_{-0.5}^{0.5}(x_{1M}+0.5)dx \quad (30)$$

$$\int_{0.5}^{1.5}(ax^2+bx+c+0.5)dx=\int_{0.5}^{1.5}(x_{1R}+0.5)dx \quad (31)$$

The following equations are solved:

$$a=\frac{x_{1L}-2x_{1M}+x_{1R}}{2} \quad (32)$$

$$b=\frac{x_{1R}-x_{1L}}{2} \quad (33)$$

$$c=\frac{13}{12}x_{1M}-\frac{x_{1L}+x_{1R}}{24} \quad (34)$$

Then, the edge sub-pixel coordinates are (0, c).

IV. EXPERIMENTAL RESULTS AND ANALYSIS

A. IMAGE FILTERING PERFORMANCE

The effects of removing background interference information, such as nebulae and galaxies, are analyzed. For illustration, we use the following calculation for the convolved matrix I_{cove}:

$$I'_{cove}(i,j)=\begin{cases}0, & if\ I_{cove}(i,j)\le 0\\ C\cdot I_{cove}(i,j), & else\end{cases} \quad (35)$$

where C represents the normalization coefficient.

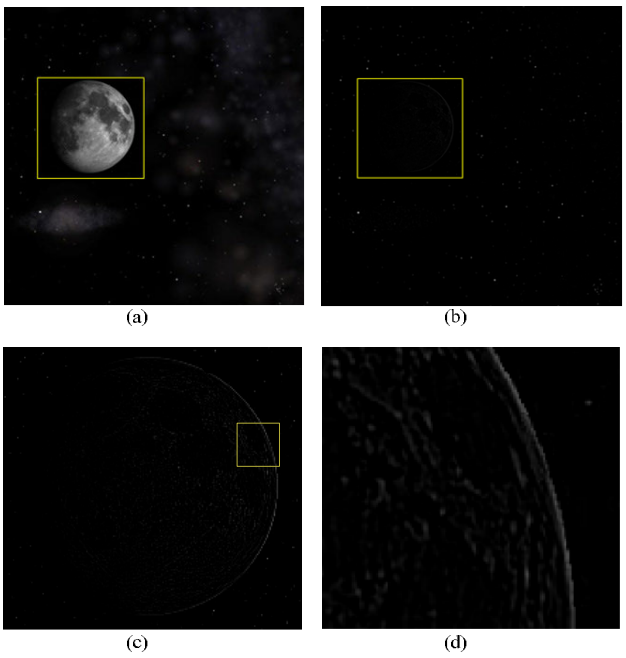

FIGURE 9. (a) Original image; (b) I'_{cove}; (c) enlarged nearby celestial body section of (b); (d) enlarged edge section of (c).

Fig. 9(a) shows the original image. Fig. 9(b) shows I'_{cove}, Notably, the interference information in the background is eliminated, and the features are preserved. Clear edge information is shown in Fig. 9(c) and Fig. 9(d). Edge information is preserved, and most surface textures are eliminated. However, but some surface textures still exist.

B. STAR FEATURE EXTRACTION PERFORMANCE

Experiments are performed using simulated images because the position of the star in the real image is unknown [21]. The star centroid error e_{cen} is used as the evaluation parameter, which is defined as the Euclidean distance between the calculated centroid $(\hat{x}_c, \hat{y}_c)$ and the true centroid (x_c, y_c):

$$e_{cen}=\left[(\hat{x}_c-x_c)^2+(\hat{y}_c-y_c)^2\right]^{1/2} \quad (36)$$

The proposed algorithm is verified by a series of star images with different brightness levels and different noise levels, and compared with the centroid method [11], Gaussian fitting method [9] and the synchronous extraction method mentioned in [21]. The Gaussian radius is set to 0.671.

1) DIFFERENT BRIGHTNESS LEVEL

The brightness level of the star centroid is specified as 1 when saturated. The extraction error of the brightness level in the range of 0.1–1.5 is analyzed at intervals of 0.05. Each simulated image contains 100 stars of the same brightness, and the position of the star centroid is evenly distributed in [−0.5, 0.5) pixels at intervals of 0.05 pixels. The star image for each brightness produces 1000 images, and the average error is calculated. Gaussian white noise with a variance of 0.001 is added to each image. The error curves are shown in Fig. 10.

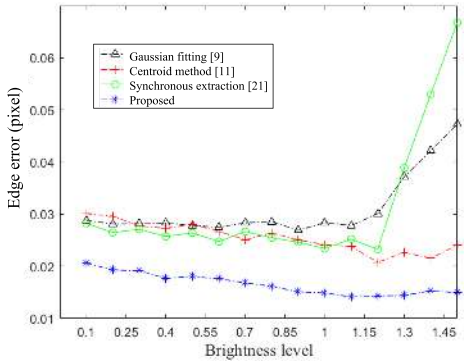

FIGURE 10. Star centroid error under different brightness level.

When the star centroid pixel is not saturated, the accuracy of the star centroid extraction increases as the brightness increases. When the star centroid pixel is overexposed, the star intensity distribution is an incomplete Gaussian function with the top removed, and the error of the centroid and synchronous extraction methods increases rapidly. The Gaussian fitting method removes the influence of overexposed pixels. Our method is based on the principle of star isotropic and symmetrical, and the effect of truncated pixels is minimal.

2) DIFFERENT NOISE LEVEL

This section analyzes the effect of different noises. Each simulated image contains 100 stars with a brightness level of 0.6, and the star centroid position is evenly distributed in [−0.5, 0.5) pixels at intervals of 0.05 pixels. The simulated

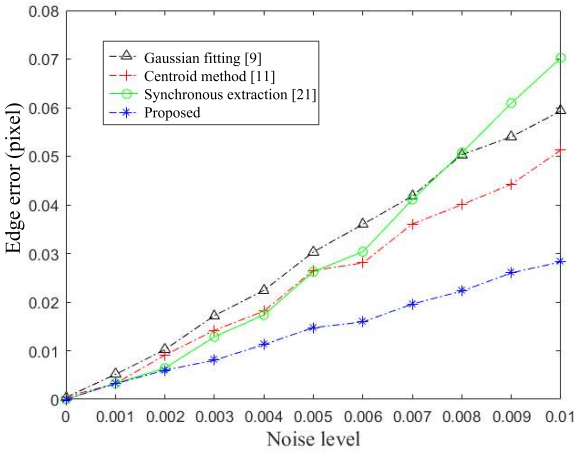

FIGURE 11. Star centroid error under different level of the noise.

image is added with Gaussian white noise with variance range of [0.001, 0.01] at intervals of 0.001. For each variance noise, 1000 images are simulated, and their average error is calculated. The error curves are shown in Fig. 11.

When the noise increases, the errors of the four methods increase accordingly. However, compared with the error increase trends of the three other methods, that of our method is relatively slow. When the noise variance is 0.01, the average error of our method is 0.0286 pixels.

C. NEARBY CELESTIAL BODY FEATURE EXTRACTION PERFORMANCE

The edge error e_{edge} is used as an evaluation parameter, which is defined as the Euclidean distance between the calculated edge coordinates $(\hat{x}_e, \hat{y}_e)$ and the true edge coordinates (x_e, y_e):

$$e_{edge} = \left[\left(\hat{x}_e - x_e\right)^2 + \left(\hat{y}_e - y_e\right)^2\right]^{1/2} \tag{37}$$

The proposed algorithm is verified by brightness level, locations, and noise level and is compared with Canny [7], Zernike [15] and synchronous extraction methods [21]. The Gaussian radius is set to 0.671.

1) DIFFERENT BRIGHTNESS LEVEL

We specify that the nearby celestial body brightness level is:

$$A = max(I_{planet})/255 \tag{38}$$

where $\max(I_{planet})$ represents the maximum gray value of nearby celestial body. Fig. 12(a) shows a simulated nearby celestial body image with Gaussian white noise, and the noise variance is 0.005. The red curve represents the circular arc of the nearby celestial body, and we count the extraction error of the edge points in the order indicated by the yellow arrows. Figs. 12(b)-12(f) show the edge error distribution for the brightness levels of 1, 0.8, 0.6, 0.4, and 0.2, respectively.

As the brightness level decreases, the edge extraction errors of all methods increase. Given that the signal-to-noise ratio decreases correspondingly as the nearby celestial body

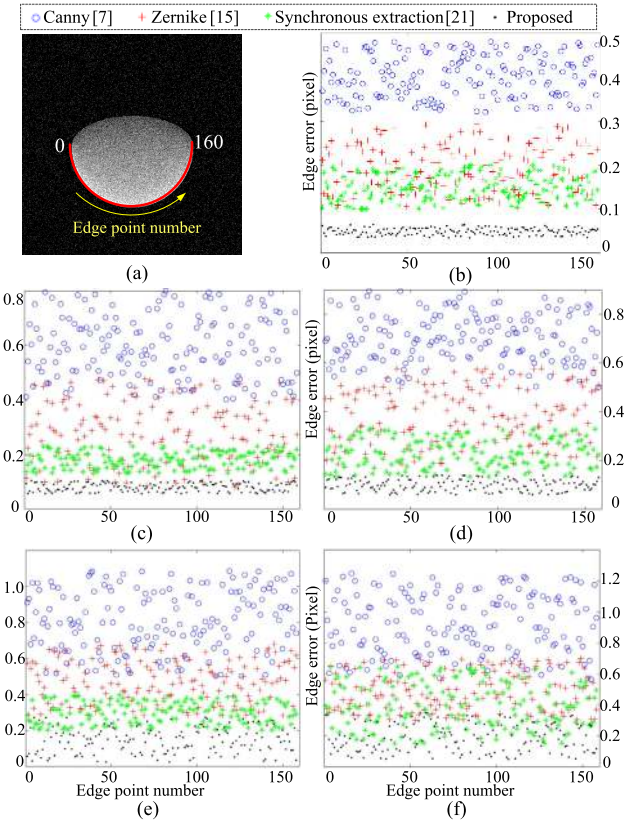

FIGURE 12. Edge error under different brightness levels. (a) simulation image; (b)–(f) edge error distribution for the brightness levels of 1, 0.8, 0.6, 0.4, and 0.2, respectively.

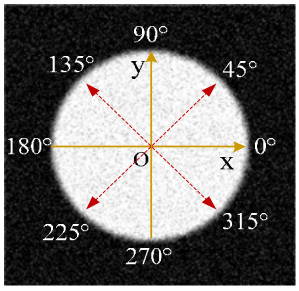

FIGURE 13. Simulation image.

brightness level decreases, the effect of noise on the algorithm increases. The accuracy of our method is still higher than those of the three other methods. At brightness level A = 0.2 the average error of our method is 0.1894 pixels.

2) DIFFERENT LOCATIONS

A circle that satisfies the blurred edges is simulated, as shown in Fig. 13, to verify the edge error at different locations. The brightness level is 0.7, and the noise variance is 0.005. The cartesian coordinate system is established with the center of the circle as the origin.

Fig. 14 shows the error distribution of the edge points; the farther from the origin of the coordinates, the larger the error of the edge points in this direction. The average error of our

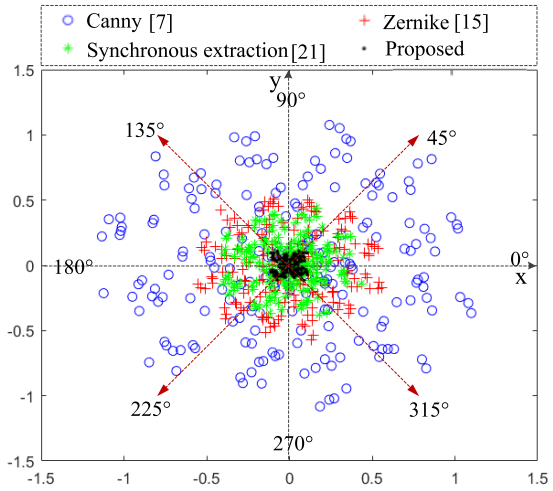

FIGURE 14. Edge error distribution.

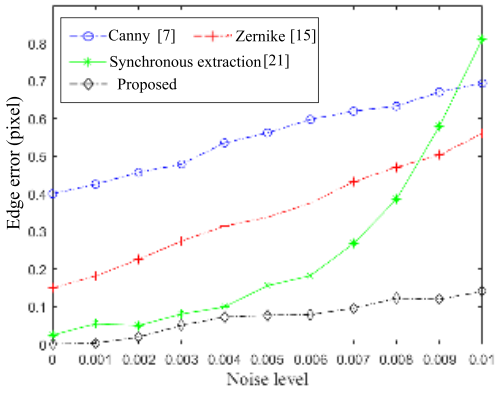

FIGURE 15. Edge error under different levels of the noise.

method is 0.0971 pixels, which is significantly lower than those of the three other methods. The error distribution of the three other methods is relatively uniform, and the error is unaffected by the position of the edge points. However, the edge error of our method is large in the directions of 45°, 135°, 225°, and 315°, and the error is small in other directions. The reason is that the local area template selects only the horizontal and vertical directions, which are not gradient directions, to save computation time and memory space but can obtain high precision for edge points in these directions.

3) DIFFERENT NOISE LEVEL

The image in Fig. 12(a) is used in the simulation to verify the effect of different noise levels on edge error. The simulated image is added with Gaussian white noise with the variance range of [0.001, 0.01] at intervals of 0.001. For each variance noise, 1000 images are simulated, and their average error is calculated. The error curves are shown in Fig. 15.

As the noise continues to increase, the error of each method increases accordingly. When the variance of the noise is greater than 0.005, the error of the synchronous extraction method increases rapidly. The reason is that the core of the synchronous extraction method is the second-order derivation of the image, which is very sensitive to noise. Compared with the errors of the three other methods, that of our method increases relatively slowly as the noise increases. This performance indicates that our method is robust to noise.

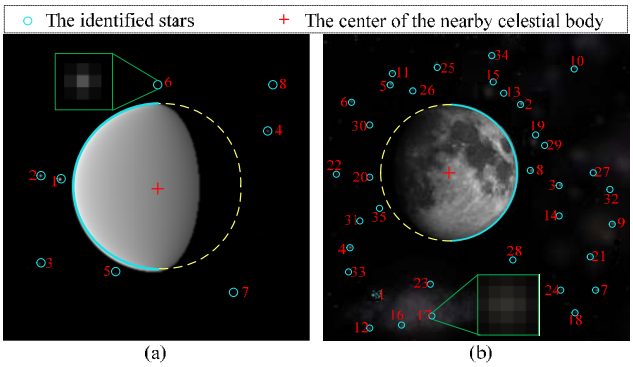

FIGURE 16. Result of star centroid and edge extraction in the simulated image.

TABLE 1. Centroid errors of the extracted stars.

No.	Ours	Method of [21]
1	0.0019	0.0647
2	0.0026	0.0798
3	0.0025	0.0958
4	0.0117	0.0490
5	0.0135	0.0327
6	0.0246	0.0385
7	0.0299	0.0995
8	0.0835	0.1029

D. SYNCHRONOUS EXTRACTION PERFORMANCE

The simulated image containing the nearby celestial body and stars is verified. The edge points are fitted by the least square method to obtain the center of the nearby celestial body. Fig. 16(a) shows a simulated image based on the light intensity models. The center error of nearby celestial body is 0.0137 pixels. Using the method of [21], the center error is 0.1092 pixels. Eight stars are extracted, and their centroid errors are shown in Table 1.

Fig. 16(b) shows an image simulated using Celestia software [37]. The information provided by the software is only the center coordinates of the moon [15]. Using our method, a total of 35 stars are extracted, the center error is 0.0786 pixels. Using the method of [21], under background interference Stars (12, 16, 17, 23, and 27) and faint Stars (21 and 33) are not extracted, and center error is 0.1273 pixels. The extracted stars are shown in Table 2.

We use the method proposed in [20] to image the moon and stars based on the ground. Fig. 17(a) contains the small and weak stars, and Fig. 17(b) contains the moon and stars. The configuration of the navigation sensor hardware is as follows: focal length is 100 mm; FOV is 18° × 14°; aperture

TABLE 2. The extracted stars and centroid positions.

No.	Ours	Method of [21]
1	(109.3115, 535.4121)	(108.9865, 534.8516)
2	(409.0714, 143.0637)	(409.8829,142.7515)
⋮	⋮	⋮
12	(98.6983, 607.5538)	——
13	(377.3001, 122.0132)	(377.8001, 121.7063)
14	(498.9314, 369.9018)	(498.7385, 370.6424)
15	(353.4106, 96.5760)	(352.2224, 96.0308)
16	(165.8680, 601.0923)	——
17	(225.3575, 581.1943)	——
⋮	⋮	⋮
32	(594.6978, 320.9899)	(594.2997, 320.1209)
33	(53.3110, 490.9004)	——
34	(351.0499, 45.4027)	(351.8841, 45.0940)
35	(117.3424, 358.0689)	(117.7445, 358.8280)

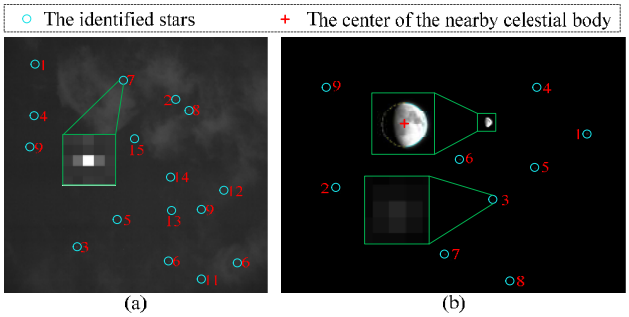

FIGURE 17. Result of features extraction of stars and moon based on ground observation.

TABLE 3. The extracted stars and centroid positions of the actual image.

No.	Ours	Method of [21]
1	(46.2735, 41.0928)	(46.8403, 41.4872)
2	(260.9798, 99.3639)	——
3	(112.2655, 326.8404)	(112.6286, 327.5075)
4	(46.2952, 122.0853)	(45.4870, 121.7609)
5	(172.6869, 283.7238)	(173.8585, 284.1356)
6	(251.3359, 347.0849)	——
7	(182.9574, 66.1429)	——
8	(282.4254, 114.0433)	——
9	(302.2094, 268.1991)	(302.2321, 268.5583)
10	(131.2547, 193.3909)	(130.9466, 193.8680)
11	(300.0009, 374.1935)	——
12	(333.9422, 239.6363)	——
13	(256.1551, 269.6386)	(256.1705, 269.9388)
14	(253.6626, 217.6493)	(254.0994, 217.0238)
15	(197.1192, 158.6351)	——

is 45 mm; image sensor is CMV20000; image resolution is 5120 × 3840 pixels. Fig. 17 is the result of feature extraction of stars and moon based on ground observation.

As shown in Fig. 17(a), using our method, a total of 15 stars are extracted. Using the method of [21], the Stars of 2, 6, 7, 8, 11,12, and 15 are not extracted. The extracted stars of Fig. 17(a) are shown in Table 3.

In Fig. 17(b), a total of 9 stars are extracted using our method. However, using the method of [21], faint Stars of 3 and 8 are not extracted. The extracted stars of Fig. 17(b) are shown in Table 4.

TABLE 4. The extracted stars and centroid positions of the actual image.

No.	Ours	Method of [21]
1	(468.3819, 148.8763)	(468.4814, 149.6888)
2	(83.1692, 233.6909)	(83.3522, 233.6889)
3	(324.6904, 252.9283)	——
4	(391.8689, 75.9820)	(392.3436, 76.3507)
5	(387.9607, 200.6206)	(388.3903, 200.0134)
6	(274.4816, 188.5895)	(273.1360, 188.7043)
7	(250.6564, 336.7262)	(250.5096, 336.7735)
8	(351.3555, 378.8846)	——
9	(71.1448, 78.0830)	(71.3357, 77.0023)

V. CONCLUSION

In this study, a high-precision and strong robustness synchronous feature extraction algorithm for different celestial bodies is provided for deep space exploration OPNAV. This algorithm is mainly used to extract the centroid of star and the edge of nearby celestial body. The ring filter template effectively removes background interference information of background and highlights feature points. According to the SDD and specific area characteristics, the features are initially extracted and distinguished. The sub-pixel-level precision of the features is simultaneously extracted based on 1D energy deviation effect in the local area template. Simulation and ground-based experiments verify the accuracy and robustness of our algorithm. The effects of different brightness levels and noise on star centroid estimation and edge extraction accuracy are analyzed. For the edges of different gradient directions, the extraction errors of the edges of varying position pairs have a great influence. The error curves of these influencing factors show that the performance of this algorithm is better than that of other algorithms. The model is a high-precision and robust feature extraction algorithm for OPNAV systems. The proposed algorithm also has certain reference significance for small and weak target detection and edge detection in other fields, such as infrared detection, medical image, target measurement, and machine vision.

REFERENCES

[1] V. Sazdovski, A. Kitanov, and I. Petrovic, "Implicit observation model for vision aided inertial navigation of aerial vehicles using single camera vector observations," *Aerosp. Sci. Technol.*, vol. 40, pp. 33–46, Jan. 2015.
[2] J. A. Christian, "Optical navigation using planet's centroid and apparent diameter in image," *J. Guid., Control, Dyn.*, vol. 38, no. 2, pp. 192–204, 2015.
[3] J. Li, H. Cui, and Y. Tian, "Nonlinearity analysis of measurement model for vision-based optical navigation system," *Acta Astronautica*, vol. 107, pp. 70–78, Feb./Mar. 2015.
[4] J. A. Christian, "Optical navigation for a spacecraft in a planetary system," Ph.D. dissertation, Dept. Aerosp. Eng., Texas Univ., Austin, TX, USA, 2010.
[5] Y. Yang, C. Zhang, J. Lu, and H. Zhang, "Classification of methods in the SINS/CNS integration navigation system," *IEEE Access*, vol. 6, pp. 3149–3158, 2018.
[6] G. Wang, W. Lv, J. Li, and X. Wei, "False star filtering for star sensor based on angular distance tracking," *IEEE Access*, vol. 7, pp. 62401–62411, 2019.
[7] S. Li, R. Lu, L. Zhang, and Y. Peng, "Image processing algorithms for deep-space autonomous optical navigation," *J. Navigation*, vol. 66, no. 4, pp. 605–623, 2013.
[8] M. R. Shortis, T. A. Clarke, and T. Short, "Comparison of some techniques for the subpixel location of discrete target images," *Proc. SPIE*, vol. 2350, pp. 239–250, Oct. 1994.

[9] T. Delabie, J. De Schutter, and B. Vandenbussche, "An accurate and efficient Gaussian fit centroiding algorithm for star trackers," *J. Astron. Sci.*, vol. 61, no. 1, pp. 60–84, Mar. 2014.
[10] H. Zhang, Y. Su, L. Yang, J. Shang, C. Liu, J. Wang, S. Zhou, Z. Jiang, and Z. Zhang, "Star detection and accurate centroiding for the geosynchronous interferometric infrared sounder of fengyun-4A," *IEEE Access*, vol. 7, pp. 18510–18520, 2019.
[11] W. Xu, Q. Li, H.-J. Feng, Z.-H. Xu, and Y.-T. Chen, "A novel star image thresholding method for effective segmentation and centroid statistics," *Optik*, vol. 124, no. 20, pp. 4673–4677, 2013.
[12] D. R. Thompson, M. Bunte, R. Castaño, S. Chien, and R. Greeley, "Image processing onboard spacecraft for autonomous plume detection," *Planet. Space Sci.*, vol. 62, no. 1, pp. 153–159, Mar. 2012.
[13] K.-J. Park and D. Mortari, "Planet or Moon image processing for spacecraft attitude estimation," *J. Electron. Imag.*, vol. 17, no. 2, pp. 023020-1–023020-11, Apr. 2008.
[14] C. Pingyuan, Y. Fuzhan, and C. Hutao, "Attitude and position determination scheme of lunar rovers basing on the celestial vectors observation," in *Proc. IEEE Int. Conf. Integr. Technol. (ICIT)*, Mar. 2007, pp. 538–543.
[15] S. Du, M. Wang, X. Chen, S. Fang, and H. Su, "A high-accuracy extraction algorithm of planet centroid image in deep-space autonomous optical navigation," *J. Navigation*, vol. 69, pp. 828–844, Jul. 2016.
[16] J. A. Christian, "Accurate planetary limb localization for image-based spacecraft navigation," *J. Spacecraft Rockets*, vol. 54, no. 3, pp. 708–730, 2017.
[17] M. Wang, Y. Cheng, B. Yang, S. Jin, and H. Su, "On-orbit calibration approach for optical navigation camera in deep space exploration," *Opt. Express*, vol. 24, no. 5, pp. 5536–5554, 2016.
[18] D. Mortari, C. N. D'Souza, and R. Zanetti, "Image processing of illuminated ellipsoid," *J. Spacecraft Rockets*, vol. 53, no. 3, pp. 448–456, 2013.
[19] S. Wang, S. Zhang, B. Zhou, and X. Wang, "A factor graph approach for attitude estimation of spacecraft using a stellar gyroscope," *IEEE Access*, vol. 7, pp. 20060–20075, 2019.
[20] H. Wang, J. Jiang, and G. Zhang, "Celestial object imaging model and parameter optimization for an optical navigation sensor based on the well capacity adjusting scheme," *Sensors*, vol. 17, no. 4, p. 915, 2017.
[21] J. Jiang, H. Wang, and G. Zhang, "High-accuracy synchronous extraction algorithm of star and celestial body features for optical navigation sensor," *IEEE Sensors J.*, vol. 18, no. 2, pp. 713–723, Jan. 2018.
[22] C. C. Liebe, "Accuracy performance of star trackers—A tutorial," *IEEE Trans. Aerosp. Electron. Syst.*, vol. 38, no. 2, pp. 587–599, Apr. 2002.
[23] H. Zhang, Y. Su, J. Shang, L. Yang, B. Cai, C. Liu, J. Wang, S. Zhou, and Z. Zhang, "Accurate star centroid detection for the advanced geosynchronous radiation imager of fengyun-4A," *IEEE Access*, vol. 6, pp. 7987–7999, 2018.
[24] H. Jia, J. Yang, X. Li, J. Yang, M. Yang, Y. Liu, and Y. Hao, "Systematic error analysis and compensation for high accuracy star centroid estimation of star tracker," *Sci. China Technol. Sci.*, vol. 53, no. 11, pp. 3145–3152, 2010.
[25] J. Yan, J. Jiang, and G. Zhang, "Dynamic imaging model and parameter optimization for a star tracker," *Opt. Express*, vol. 24, no. 6, pp. 5961–5983, 2016.
[26] B. R. Hancock, R. C. Stirbl, T. J. Cunningham, B. Pain, C. J. Wrigley, and P. G. Ringold, "CMOS active pixel sensor specific performance effects on star tracker/imager position accuracy," *Proc. SPIE*, vol. 4284, pp. 43–53, May 2001.
[27] G. Rufino and D. Accardo, "Enhancement of the centroiding algorithm for star tracker measure refinement," *Acta Astronautica*, vol. 53, no. 2, pp. 135–147, Jul. 2003.
[28] J. Enright, "Moon-tracking modes for star trackers," *J. Guid., Control, Dyn.*, vol. 33, no. 1, pp. 171–185, 2010.
[29] M.-S. Wei, F. Xing, and Z. You, "A real-time detection and positioning method for small and weak targets using a 1D morphology-based approach in 2D images," *Light, Sci. Appl.*, vol. 7, May 2018, Art. no. 18006.
[30] S. C. Loke, "Astronomical image acquisition using an improved track and accumulate method," *IEEE Access*, vol. 5, pp. 9691–9698, 2017.
[31] A.-G. Zhao, H.-L. Wang, X.-G. Yang, J.-H. Lu, W. Jiang, and N. Qi, "Infrared small-target detection using the maximum of second-order directional derivative," *Chin. J. Lumin.*, vol. 37, no. 9, pp. 1142–1151, 2016.
[32] N. Wang, Y. Shang, Y. Chen, M. Yang, Q. Zhang, Y. Liu, and Z. Gui, "A hybrid model for image denoising combining modified isotropic diffusion model and modified Perona-Malik model," *IEEE Access*, vol. 6, pp. 33568–33582, 2018.
[33] P. Chen, F. Chen, Y. Han, and Z. Zhang, "Sub-pixel dimensional measurement with Logistic edge model," *Optik*, vol. 125, no. 9, pp. 2076–2080, May 2014.
[34] J. Ye, G. Fu, and U. P. Poudel, "High-accuracy edge detection with blurred edge model," *Image Vis. Comput.*, vol. 23, no. 5, pp. 453–467, May 2005.
[35] L. Su, X. Yu, K. Li, X. Yao, and M. Pecht, "Simulation and experimental verification of edge blurring phenomenon in microdefect inspection based on high-frequency ultrasound," *IEEE Access*, vol. 7, pp. 11515–11525, 2019.
[36] A. Trujillo-Pino, K. Krissian, M. Alemán-Flores, and D. Santana-Cedrés, "Accurate subpixel edge location based on partial area effect," *Image Vis. Comput.*, vol. 31, no. 1, pp. 72–90, 2013.
[37] Celestia. *The Celestia Motherlode*. Accessed: Mar. 31, 2018. [Online]. Available: http://www.celestiamotherlode.net/

YONG ZHANG was born in Yuncheng, China, in 1989. He received the B.S. degree in optical information science and technology from Shanxi University, in 2012, and the M.E. degree from the College of Science, China University of Petroleum, in 2015. He is currently pursuing the Ph.D. degree with the School of Instrumentation Science and Opto-Electronics Engineering, Beihang University. His main research interests include optical navigation and precision measurement.

JIE JIANG received the bachelor's, master's, and Ph.D. degrees from Tianjing University, in 2000. She is currently a Professor with the School of Instrumentation Science and Opto-Electronics Engineering, Beihang University (BUAA), China. Her research interests include image processing and star sensors.

GUANGJUN ZHANG received the Ph.D. degree from the Department of Precision Instrumentations Engineering, Tianjin University, China, in 1991. He was a Visiting Professor with North Dakota State University, USA, from 1997 to 1998. He is currently a Professor with the School of Instrumentation Science and Opto-Electronics Engineering, Beihang University, China. He is also an Academician of the Chinese Academy of Engineering. His research interests include laser precision measurement, machine vision, optical sensing, and artificial intelligence.

YAN LU received the B.S. degree from the Department of Physics from East China Normal University, in 2008, and the M.E. degree from the Department of Physics, China University of Petroleum, in 2014. She is currently pursuing the Ph.D. degree with the School of Instrumentation Science and Opto-Electronics Engineering, Beihang University. Her main research interests include inertial navigation and precision measurement.